Control Engineering Practice 26 (2014) 82–90

Contents lists available at ScienceDirect

Control Engineering Practice

journal homepage: www.elsevier.com/locate/conengprac

Two-sensor control in active vibration isolation using hard mounts

Michiel A. Beijen [a,*], Dirk Tjepkema [b], Johannes van Dijk [a]

[a] University of Twente, Department of Mechanical Automation and Mechatronics, NL-7500 AE Enschede, The Netherlands
[b] Demcon Advanced Mechatronics, Institutenweg 25, NL-7521 PH Enschede, The Netherlands

ARTICLE INFO

Article history:
Received 24 June 2013
Accepted 28 December 2013
Available online 8 February 2014

Keywords:
Active vibration isolation
Vibration control
Hard mount
Two-sensor control

ABSTRACT

To isolate precision machines from floor vibrations, active vibration isolators are often applied. In this paper, a two-sensor control strategy, based on acceleration feedback and force feedback, is proposed for an active vibration isolator using a single-axis active hard mount. The hard mount provides a stiff support while an active control system is used to get the desired isolation performance. In our previous work, we showed that a sensor fusion control strategy for active hard mounts can be used to realize three performance objectives simultaneously: providing isolation from floor vibrations, achieving a low sensitivity for direct disturbance forces, and adding damping to internal modes of the supported precision machine. In the present work, an enhanced control strategy is presented, referred to as two-sensor control. We will show that two-sensor control outperforms sensor fusion, because it has more possibilities for loop-shaping and has better stability properties. The two-sensor control strategy is successfully validated on an experimental setup.

© 2014 Elsevier Ltd. All rights reserved.

1. Introduction

Vibration isolators are widely used in high-precision machines (e.g. wafer scanners) (Heertjes, de Graaff, & van der Toorn, 2005). Passive isolators consist of physical springs and dampers between the floor and the supported machine (Rivin, 2003). Such isolators can only reach a limited performance because a large passive damping of the suspension mode leads to less vibration isolation at high frequencies (Karnopp & Trikha, 1969). Active isolators contain, in addition to physical springs, a control system to realize active vibration control.

For vibration isolators in general it holds that vibration isolation is obtained above $\sqrt{2}$ times the system's suspension frequency, which is calculated as the square root of the support stiffness divided by the supported mass. To obtain a low suspension frequency (typically 1–2 Hz) the machine is usually mounted on low-stiffness springs, the so-called soft mounts (Heertjes et al., 2005). However, the low support stiffness introduces leveling problems, and it also makes the machine susceptible to direct disturbance forces (e.g. caused by cables, accelerating stages, etc.) (van der Poel, 2010). An alternative approach is using active hard mounts (Beard, Schubert, & von Flotow, 1994; Nelson, 2002; Tjepkema, van Dijk, & Soemers, 2011; van der Poel, 2010), which provide a much stiffer support. Due to the higher suspension frequency (typically 10–20 Hz) the transmissibility of floor vibrations must be actively reduced to make it comparable to that of soft mounts (Tjepkema et al., 2011). A consequence of actively reducing the suspension frequency is that internal modes are also lowered in frequency and remain poorly damped (Tjepkema et al., 2011; van Dijk, 2009). Poorly damped internal modes result in a relatively large internal deformation and settling time, and as a consequence a relatively large misalignment within the machine (Holterman & de Vries, 2004).

To improve the performance of active hard mounts, we present a two-sensor control strategy that satisfies three performance objectives simultaneously: (1) realizing a low-frequency and well-damped suspension mode to obtain a low transmissibility of floor vibrations, (2) providing a stiff support, and (3) increasing the damping of internal modes. We will show that we can damp internal modes of active hard mounts by damping the anti-resonances in the control loop. We will show also that this is not possible when only a single sensor is used. The two-sensor control strategy results always in a stable system as long as the sensors and actuators are collocated. The controller needs no prior knowledge of the internal modes, therefore no detailed model is needed and model uncertainties do not limit the performance of the controller. The two-sensor control strategy presented in this paper is developed from the sensor fusion control strategy presented in our previous work (Tjepkema et al., 2011). Using sensor fusion, the outputs of an accelerometer and a force sensor are merged and fed back to a single-input single-output (SISO) controller. Using two-sensor control, separated feedback controllers are designed for each sensor signal, resulting in a multiple-input–single-output (MISO) controller.

* Corresponding author. Tel.: +31 53 489 2502.
E-mail address: m.a.beijen@alumnus.utwente.nl (M.A. Beijen).

0967-0661/$ - see front matter © 2014 Elsevier Ltd. All rights reserved.
http://dx.doi.org/10.1016/j.conengprac.2013.12.015

Therefore two-sensor control has more possibilities for loop shaping and better stability properties.

Two-sensor control by combining absolute motion feedback (e.g. using a geophone or accelerometer) and force feedback has already been used in several applications for vibration isolation. Among others, Gardonio, Elliott, and Pinnington (1997) studied the combination of velocity feedback and force feedback to reduce the structural power transmission from a vibrating source to a receiving plate. Hauge and Campbell (2004) used two-sensor control for vibration isolation in aerospace equipment to profit from the low-frequency performance of a geophone and the high-frequency robustness of a load cell. Pantazi, Sebastian, Pozidis, and Eleftheriou (2005) used two-sensor-based H_∞ control such that they can use different sensors for the low- and high-frequency range to determine the position of a probe storage. El-Sinawi (2004) and van der Poel (2010) use two-sensor control to realize a feedforward-feedback controller for active vibration isolation, using a floor sensor for feedforward and a machine sensor for feedback control. However, none of the two-sensor control strategies described in these references can be used directly for simultaneously realizing the three mentioned performance objectives as mentioned above. Therefore we present in this paper a two-sensor control strategy which specifically aims at simultaneously realizing these three performance objectives.

This paper is organized as follows. Section 2 describes the limitations of single-sensor control. The two-sensor control strategy is explained and compared to sensor fusion in Section 3. The validation of the proposed control strategy on an experimental setup is described in Section 4. Sections 5 and 6 present a discussion and the conclusions, respectively.

2. Feedback control using a single sensor

This section starts with a description of the plant model for active hard mounts and a definition of the performance objectives. Subsequently the controllers for single-sensor control are designed. The section ends with discussing the limitations of single-sensor control.

2.1. Description of the plant

To model a machine supported by an active vibration isolator, a rigid-body model can be used as shown in Fig. 1. The model consists of a rigid body with machine mass m on a hard mount with stiffness k_1. The actuator produces a force F_a and is assumed to behave as an ideal actuator within the bandwidth of the controller. The position of m can be disturbed by a floor motion x_0 (broadband floor vibrations) and a direct disturbance force F_d (originating from moving stages, acoustical noise, etc.). Since practical vibration isolators contain parasitic stiffness paths (e.g. originating from cables and guidances), a small parasitic stiffness k_p is taken into account. Measurements are taken from an accelerometer $\ddot{x}_1$ on m and a force sensor F_s located between the mount and m. The stiffness of the force sensor is considered to be infinite. No physical damper is present since the suspension mode is actively damped and the mechanical damping of a physical spring is assumed to be negligible. It is assumed that the floor can be considered as an ideal displacement source. Since precision machines are usually placed on stiff and heavy floors, the effect of the actuator force F_a on the floor displacement is negligible, which justifies this assumption (van der Poel, 2010).

To model an internal mode of the machine, a flexible-body model, as in Fig. 2, can be used. Therefore the supported machine mass m is split into two separate masses m_1 and m_2 connected by a spring with stiffness k_2. Numerical values for this model are listed in Table 1. These numbers correspond to the values of the experimental setup used in Section 4. With these values of the masses and the stiffnesses, the suspension frequency of the machine is 13 Hz, while the internal mode has a resonance frequency of 93 Hz. This suspension frequency is typically for an active hard mount vibration isolator (Tjepkema et al., 2011) and 93 Hz is typical for a first resonance frequency of the internal mode of a precision machine (Holterman & de Vries, 2004). A parasitic stiffness of 1% of the value of suspension stiffness k_1 is taken into account. Table 1 also contains numerical values for an ideal soft mount system, which will be used as a reference system. The ideal active soft mount system has a suspension frequency of 1 Hz with 70% skyhook damping (Tjepkema et al., 2011).

2.2. Performance objectives

To analyze the performance of the vibration isolator, three transfer functions are defined as performance objectives. The first function is the transmissibility, describing the response of the machine to floor vibrations:

$$T(s) \equiv \frac{\ddot{X}_1(s)}{\ddot{X}_0(s)}. \tag{1}$$

Note that $\ddot{X}_1(s)$ is a short notation for $s^2X_1(s)$. The second function is the compliance, describing the response of the machine to direct disturbance forces:

$$C(s) \equiv \frac{X_1(s)}{F_d(s)}. \tag{2}$$

The third function is the deformation transmissibility, describing the response of internal machine deformations ($\Delta X(s) = X_2(s) - X_1(s)$) due to floor vibrations:

$$T_d(s) \equiv \frac{\Delta X(s)}{\ddot{X}_0(s)}. \tag{3}$$

A high deformation transmissibility leads to internal deformations, and thus performance limitation because of misalignment in the machine.

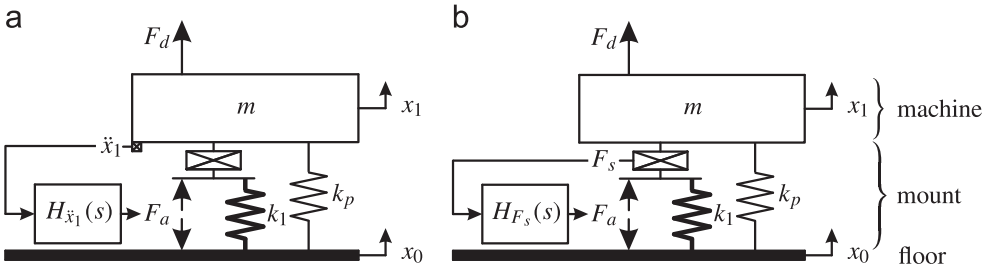

Fig. 1. Rigid-body model for active vibration isolation with (a) acceleration feedback and (b) force feedback. The active hard mount is modeled as an actuator force F_a and a high-stiffness spring k_1. Mass m represents the suspended machine, spring k_p represents a parasitic stiffness.

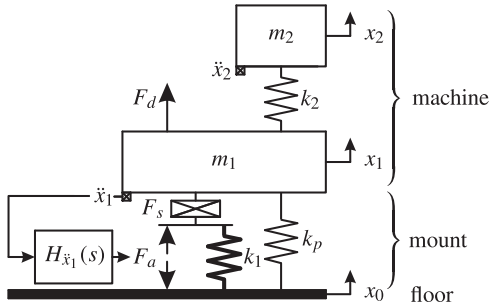

Fig. 2. Flexible-body model, containing one internal mode (acceleration feedback). In contrast with the rigid-body model from Fig. 1, the machine is modeled now as two masses, m_1 and m_2, connected by an internal machine stiffness k_2.

Table 1
Mass and stiffness properties of hard and soft mount systems.

System	m_1 (kg)	m_2 (kg)	k_1 (N/m)	k_2 (N/m)	k_p (N/m)
Hard mount	2.8	2.6	36 000	450 000	360
Soft mount	2.8	2.6	213	450 000	0

2.3. Controller design

This section describes the controllers for single-sensor control using either acceleration or force feedback. The controllers are used to lower the suspension frequency of the hard mount and to add damping to the suspension mode.

2.3.1. Acceleration feedback

For acceleration feedback by measuring $\ddot{x}_1$, the following PI controller can be used to fulfill the requirements (Tjepkema et al., 2011):

$$H_{\ddot{X}_1}(s)=\frac{F_a(s)}{\ddot{X}_1(s)}=-\left(K_a+\frac{K_v}{s}\right). \tag{4}$$

A physical interpretation of this PI controller is the addition of virtual mass by the proportional (P) action to lower the suspension frequency, and virtual sky-hook damping by the integral (I) action to damp the suspension mode (van Dijk, 2009). The numerical values for K_a and K_v depend on the desired closed loop transmissibility, i.e. the closed loop suspension frequency and its relative damping. Therefore an expression for the closed loop transmissibility is derived first. The derivation starts with the Laplace transform of the equation of motion for the rigid-body model (Fig. 1):

$$(ms^2+k_1+k_p)X_1(s)=(k_1+k_p)X_0(s)+F_a(s)+F_d(s). \tag{5}$$

Next, substitute $F_a(s)=H_{\ddot{X}_1}(s)\ddot{X}_1(s)$ in (5), with $H_{\ddot{X}_1}(s)$ as given in (4). After this substitution, the following transmissibility function is obtained for the closed loop system with acceleration feedback:

$$T(s)=\frac{\dfrac{k_1+k_p}{m+K_a}}{s^2+\dfrac{K_v}{m+K_a}s+\dfrac{k_1+k_p}{m+K_a}}. \tag{6}$$

This transfer function can also be written as

$$T(s)=\frac{\omega_n^2}{s^2+2\zeta_n\omega_n s+\omega_n^2}. \tag{7}$$

From (6) and (7), the closed loop suspension frequency ω_n and its relative damping ζ_n are derived:

$$\omega_n=\sqrt{\frac{k_1+k_p}{m+K_a}}, \tag{8}$$

$$\zeta_n=\frac{K_v}{2\omega_n(m+K_a)}. \tag{9}$$

From (8) and (9) it follows that the closed loop parameters ω_n and ζ_n can be set to any desired value by choosing the appropriate values for K_a and K_v. We choose $\omega_n=1\cdot 2\pi$ rad/s and $\zeta_n=0.7$ to make the transmissibility of an active hard mount system comparable to that of an ideal soft mount system. Given these control objectives, the controller parameters are calculated by rewriting (8) and (9) and using the numerical values from Table 1:

$$K_a=\frac{k_1+k_p}{\omega_n^2}-m=9.2\times 10^2, \tag{10}$$

$$K_v=2\zeta_n\omega_n(K_a+m)=8.0\times 10^3. \tag{11}$$

Similar to $T(s)$, the compliance of the closed loop system with acceleration feedback can be derived from (5):

$$C(s)=\frac{1}{(m+K_a)s^2+K_v s+(k_1+k_p)}. \tag{12}$$

The static compliance ($C(s\to 0)$) equals $1/(k_1+k_p)$. This implies that the control system with acceleration feedback does not negatively affect the desired high static stiffness of the passive hard mount.

2.3.2. Force feedback

Using force feedback, the normal force measured by $F_s(s)$ can be expressed as the sum of actuator force $F_a(s)$ and the normal force in spring k_1, see Fig. 1:

$$F_s(s)=F_a(s)-k_1(X_1(s)-X_0(s)). \tag{13}$$

Combining (13) and (5) leads to an alternative expression for $F_s(s)$:

$$F_s(s)=ms^2X_1(s)+k_p(X_1(s)-X_0(s))-F_d(s). \tag{14}$$

If one neglects the contributions of k_p and F_d in (14), it follows that the sensors F_s and $\ddot{x}_1$ measure the same signals except for a gain m. Therefore controller (4), which was designed for acceleration feedback, can also be used for force feedback when it is scaled with $1/m$:

$$H_{F_s}(s)=\frac{F_a(s)}{F_s(s)}=-\frac{1}{m}\left(K_a+\frac{K_v}{s}\right). \tag{15}$$

Numerical values for K_a and K_v are directly adapted from (10) and (11), respectively. To obtain the closed loop transfer functions of $T(s)$ and $C(s)$ in the case of force feedback, substitute $F_a(s)=H_{F_s}(s)F_s(s)$ in (5), whereby an expression for $H_{F_s}(s)$ is found in (15) and an expression for $F_s(s)$ is found in (14). The closed loop transmissibility reads then

$$T(s)=\frac{\dfrac{k_1}{m+K_a}+\dfrac{k_p}{m}\left(1+\dfrac{K_v}{(m+K_a)s}\right)}{s^2+\dfrac{K_v}{m+K_a}s+\dfrac{k_1}{m+K_a}+\dfrac{k_p}{m}\left(1+\dfrac{K_v}{(m+K_a)s}\right)}. \tag{16}$$

Assuming $K_v=0$, (16) can be written in the form of (7), hence an expression for the undamped suspension frequency is obtained for the closed loop system with force feedback:

$$\omega_n=\sqrt{\frac{k_1}{m+K_a}+\frac{k_p}{m}}. \tag{17}$$

It follows from (17) that the suspension frequency is limited by the factor k_p/m when force feedback is used. The compliance for the closed loop system with force feedback equals

$$C(s)=\frac{\dfrac{1}{m}\left(1+\dfrac{K_v}{(m+K_a)s}\right)}{s^2+\dfrac{K_v}{m+K_a}s+\dfrac{k_1}{m+K_a}+\dfrac{k_p}{m}\left(1+\dfrac{K_v}{(m+K_a)s}\right)}. \tag{18}$$

For force feedback, the static compliance ($C(s\to 0)$) equals $1/k_p$. This means that for force feedback, in contrast with acceleration feedback, the control system significantly increases the static compliance. Because of the limitations in ω_n and $C(s)$ for force feedback, acceleration feedback is preferred over force feedback.

2.3.3. Stability improvement

The controllers (4) and (15) are extended with filters to improve the stability properties of the control system. To prevent actuator saturation, the controller gain is penalized by a second-order high-pass filter at 0.1 Hz ($\omega_l = 0.1\cdot 2\pi$ rad/s, $\zeta_l = 0.7$). This filter frequency is a factor 10 lower than the desired suspension frequency (1 Hz), so the filter will not influence the controller action at the suspension frequency. At high frequencies, the controller bandwidth is limited by a second-order low-pass filter to prevent stability problems due to non-modeled high-frequency dynamics and sensor noise. The corner frequency of the low-pass filter is set to 20 Hz ($\omega_f = 20\cdot 2\pi$ rad/s), resulting in an attenuation of 50 dB in the transmissibility $[(\omega_f/\omega_n)^2 = (20/1)^2 = 400 > 50$ dB]. An attenuation level of 50 dB is comparable to the attenuation provided by soft mount systems (Tjepkema et al., 2011). The relative damping ζ_f of the low-pass filter can be set to any value. In this paper $\zeta_f = 0.07$ is used. A lower value of ζ_f results in more vibration isolation in the frequency range around ω_f. Finally, a zero at 290 Hz ($\omega_z = 290\cdot 2\pi$ rad/s) is added to improve the phase margin around the high cross-over frequency, which is the frequency where the magnitude of the loop gain (explained later) is equal to one. The improved controllers for acceleration feedback and force feedback are

$$H_{\ddot{X}_1,r}(s) = -\left(K_a + \frac{K_v}{s}\right)\frac{s^2}{s^2+2\zeta_l\omega_l s+\omega_l^2}\frac{\omega_f^2}{s^2+2\zeta_f\omega_f s+\omega_f^2}\frac{s+\omega_z}{\omega_z}, \quad (19)$$

$$H_{F_s,r}(s) = \frac{1}{m_1+m_2}H_{\ddot{X}_1,r}(s). \quad (20)$$

The corresponding loop gains are

$$L_{\ddot{X}_1}(s) = G_{\ddot{X}_1}(s)H_{\ddot{X}_1,r}(s), \quad (21)$$

$$L_{F_s}(s) = G_{F_s}(s)H_{F_s,r}(s). \quad (22)$$

Expressions for the transfer functions $G_{\ddot{X}_1}(s) = \ddot{X}_1(s)/F_a(s)$ and $G_{F_s}(s) = F_s(s)/F_a(s)$ can be derived by analyzing the equations of motion of the flexible-body model in Fig. 2. The loop gains are plotted in Fig. 5.

2.4. Modeling results

In Fig. 3 the performance of hard mount systems is compared to that of an ideal soft mount system for which the values are listed in Table 1. The passive soft mount system already has a suspension frequency of 1 Hz, so its control system only has to provide sky-hook damping. This is realized by using controller (4) for the soft mount with $K_a = 0$ and K_v according to (9).

Fig. 3(a) shows the transmissibility $T(s)$. The transmissibility of the active hard mount system with acceleration feedback and the active soft mount system are comparable in the frequency range up to 20 Hz. Beyond 20 Hz, the controller action of the hard mount is cut off by the low-pass filter in (19). The transmissibility of the active hard mount system with force feedback is not as desired, since the achievable suspension frequency is limited by the parasitic stiffness, see (17).

Fig. 3(b) shows the compliance $C(s)$. Using acceleration feedback, the static compliance is $1/(k_1+k_p)$, see (12), which is as desired. Using force feedback, the static compliance is $1/k_p$, see (18). The static compliance of the soft mount is about 170 times higher than that of the hard mount.

Fig. 3(c) shows the deformation transmissibility $T_d(s)$. Compared to the soft mount, the magnitude at the resonance frequency of the internal mode of active hard mounts is much higher for both acceleration feedback (at 66 Hz) and force feedback (at 92 Hz), which is undesired. For acceleration feedback, the internal mode is lowered in frequency, which is also undesired. Both feedback strategies fail to damp the internal mode.

3. Two-sensor control (TSC)

In Section 2.2, three performance objectives for active hard mount systems are defined. Section 2.4 shows that at best only two of these objectives, i.e. a low transmissibility and a low compliance, can be satisfied simultaneously with single-sensor control. In this section, it will be shown that it is possible to satisfy all three performance objectives simultaneously when using two-sensor control (TSC). In this paper, TSC is a combination of acceleration feedback and force feedback. This section describes how TSC can be used to increase the damping of an internal mode, gives a stability analysis of TSC, and shows how TSC can be used to satisfy all three performance objectives simultaneously. At the end of this section, it is shown that TSC outperforms the sensor fusion strategy described in Tjepkema et al. (2011).

3.1. Adding damping to internal modes

Consider the closed loop system in Fig. 4. The plant transfer functions $G_{ij}(s)$, from input j to output i, can be derived from the model in Fig. 2. The plant has three inputs, i.e. a floor acceleration $\ddot{X}_0(s)$, a direct disturbance force $F_d(s)$, and an actuator force $F_a(s)$. The plant has three outputs, i.e. the accelerometer $\ddot{X}_1(s)$, the force sensor $F_s(s)$, and a virtual measurement of the internal deformation $\Delta X(s)$. From SISO control systems it is known that the closed

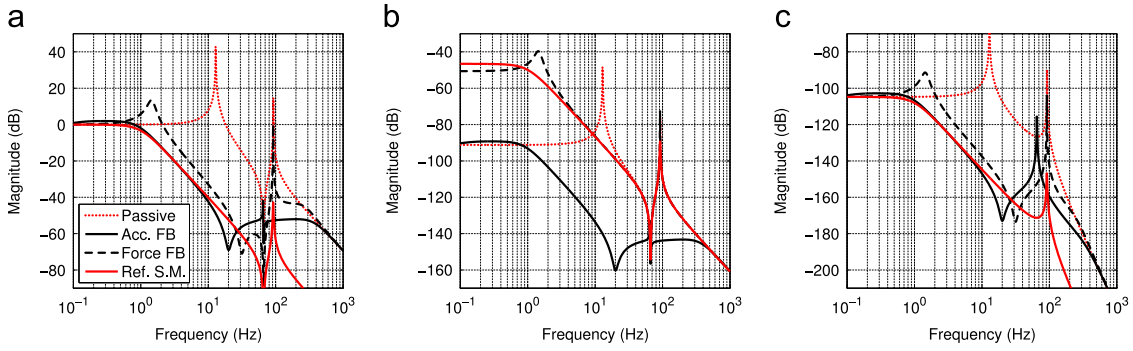

Fig. 3. Bode magnitude plot for comparing the performance of passive and active hard mount systems with the performance of an ideal soft mount (Ref. S.M.) system. The performance is assessed by means of the transmissibility (left), compliance (middle) and deformation transmissibility (right).

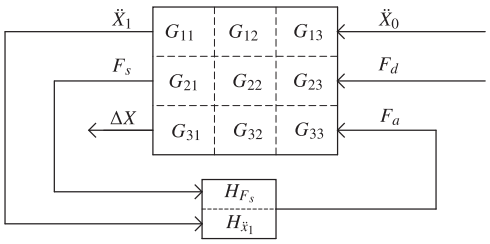

Fig. 4. Closed loop system with two-sensor control. The plant transfer functions $G_{ij}(s)$ can be derived from the model in Fig. 2; the feedback controllers are $H_{\ddot{X}_1}(s)$ and $H_{F_s}(s)$. The Laplace operator (s) has been omitted in the figure.

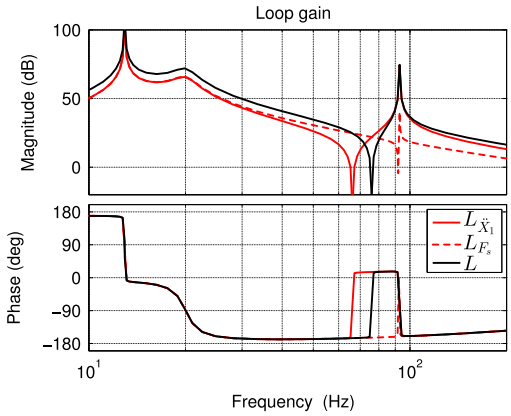

Fig. 5. Bode diagram of the loop gains for acceleration feedback (gray solid line), force feedback (gray dashed line) and the total loop gain (black solid line). Notice the different anti-resonance frequencies for acceleration feedback (66 Hz) and force feedback (92 Hz). Also notice the anti-resonance in $L(s)$ at 76 Hz, caused by the 180° phase difference between $L_{\ddot{X}_1}(s)$ and $L_{F_s}(s)$ while the gain is the same for $L_{\ddot{X}_1}(s)$ and $L_{F_s}(s)$.

loop transfer function from $\ddot{X}_0(s)$ to $\Delta X(s)$ equals the open loop transfer function $G_{31}(s)=\Delta X(s)/\ddot{X}_0(s)$ scaled with the sensitivity function $1/(1+L(s))$. In Appendix A it is shown that the same relation holds in the case of two controlled outputs:

$$\left(\frac{\Delta X(s)}{\ddot{X}_0(s)}\right)_{\text{c.l.}}=\frac{1}{1+L(s)}G_{31}(s). \tag{23}$$

where c.l. stands for closed loop, and the total loop gain $L(s)$ is the sum of $L_{\ddot{X}_1}(s)$ and $L_{F_s}(s)$ as defined by (21) and (22), respectively. From (23) it can be concluded that a high magnitude of $L(s)$ results in a strong attenuation of internal deformation. On the other hand, if $L(s)\to 0$, such as in the case of a poorly damped anti-resonance frequency, there is no active attenuation of internal deformations. Therefore, $L(s)$ should not contain poorly damped anti-resonances in the frequency range where internal modes must be damped. Fig. 5 shows the bode plots for $L_{\ddot{X}_1}(s)$ and $L_{F_s}(s)$, in the case of single-sensor control defined by (21) and (22), respectively, and the sum $L(s)=L_{\ddot{X}_1}(s)+L_{F_s}(s)$. From Fig. 5 it is observed that both $L_{\ddot{X}_1}(s)$ and $L_{F_s}(s)$ contain anti-resonances, but that they differ in frequency. The frequencies of these anti-resonances are approximated (see Tjepkema et al., 2011) as

$$\omega_{a,\ddot{X}_1}=\sqrt{\frac{k_2}{m_2}}=66\text{ Hz}, \tag{24}$$

$$\omega_{a,F_s}\approx\sqrt{\frac{k_2}{m_2}\left(1+\frac{m_2}{m_1}\right)}=92\text{ Hz}. \tag{25}$$

Fig. 5 also shows that an anti-resonance in $L(s)$ appears at 76 Hz, because at this frequency both $L_{\ddot{X}_1}(s)$ and $L_{F_s}(s)$ have the same magnitude (22 dB) but opposite sign due to a 180° phase difference. A method to circumvent such anti-resonances caused by a 180° phase difference, without precisely knowing the internal resonances of the plant, is realizing a 90° phase difference between $L_{\ddot{X}_1}(s)$ and $L_{F_s}(s)$. In the complex s-plane this is interpreted as the summation of two perpendicular vectors, which can never result in a zero value. This method is illustrated by the example in the following subsection.

3.1.1. Example: damping the internal mode

As an example, consider the controllers $H_{\ddot{X}_1,ex}(s)=10^6/\text{s}^2$ and $H_{F_s,ex}(s)=500/\text{s}$ for acceleration feedback and force feedback, respectively. The corresponding bode plots are given in Fig. 6. In this example, $H_{\ddot{X}_1,ex}(s)$ has a roll-off rate of −40 dB/decade and $H_{F_s,ex}(s)$ has −20 dB/decade. Both controllers are 90° out-of-phase in the complete frequency range. The corresponding loop gains are given in Fig. 7. In the frequency range between $\omega_{a,\ddot{X}_1}$ (66 Hz) and ω_{a,F_s} (92 Hz), the phase difference between $L_{\ddot{X}_1,ex}(s)$ and $L_{F_s,ex}(s)$ is equal to +90°, elsewhere the phase difference is −90°. From Fig. 7 it is observed that this method performs well since $L_{ex}(s)=L_{\ddot{X}_1,ex}(s)+L_{F_s,ex}(s)$ has no poorly damped anti-resonances anymore. From the theory in the previous subsection it follows that this is equivalent to adding damping to the internal modes.

This example shows that it is possible to damp anti-resonances in the control loop using two-sensor control. This is possible because the anti-resonance frequencies are not closely located to each other (66 Hz vs. 92 Hz). However, when the anti-resonance frequencies almost coincide, neither acceleration feedback nor force feedback can put a strong control action to the system at

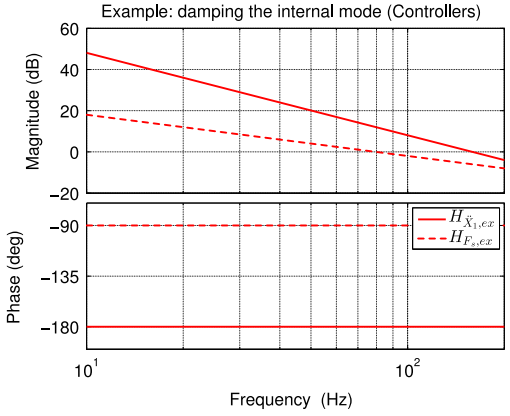

Fig. 6. Example bode diagram of an acceleration feedback controller (solid line) and a force feedback controller (dashed line) satisfying the 90° out-of-phase property. This property is used to damp internal modes of the suspended machine.

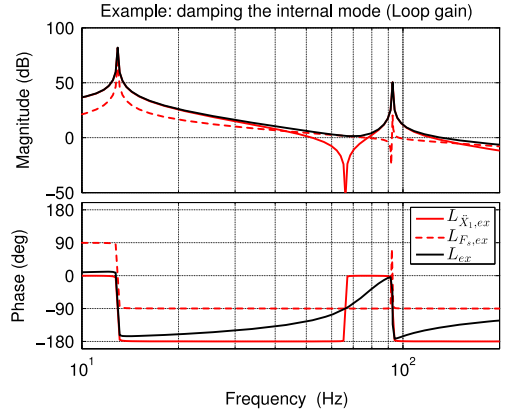

Fig. 7. Corresponding loop gains for the controllers shown in Fig. 6. $L_{\ddot{X}_1,ex}(s)$ is the loop gain for acceleration feedback, $L_{F_s,ex}(s)$ is for force feedback, and $L_{ex}(s)=L_{\ddot{X}_1,ex}(s)+L_{F_s,ex}(s)$ is for two-sensor control. It appears that $L_{ex}(s)$ has no poorly damped anti-resonance anymore, because of the 90° out-of-phase property.

that frequency. The result is that the summed loop gain will still have an anti-resonance at that specific frequency, leading to an internal mode that is still poorly damped. In our example, the anti-resonances are located far enough from each other because the mass ratio m_2/m_1 is sufficiently large.

3.2. Stability analysis

In Fig. 6, the roll-off rates are -40 dB/decade for $H_{\ddot{X}_1,ex}(s)$ and -20 dB/decade for $H_{F_s,ex}(s)$. From a stability point of view, this is the only possible combination of roll-off rates. Suppose, as an alternative, a -20 dB/decade rate for $H_{\ddot{X}_1,ex}(s)$ and a 0 dB/decade rate for $H_{F_s,ex}(s)$. Then the 90° phase difference is still achieved, but the force feedback loop has no roll-off anymore. This results in an infinite bandwidth of the force feedback loop and therefore stability problems due to higher-order dynamics and sensor noise. Another alternative could be a roll-off rate of -60 dB/decade for $H_{\ddot{X}_1,ex}(s)$ and -40 dB/decade for $H_{F_s,ex}(s)$, but this can lead to stability problems due to the crossing of the $-180°$ phase line of $L_{ex}(s)$.

Using a roll-off rate of -40 dB/decade for $H_{\ddot{X}_1,ex}(s)$ and -20 dB/decade for $H_{F_s,ex}(s)$, stability of the closed loop system is guaranteed if the sensors and actuators are collocated. A property of collocated control is that variations in the phase ϕ due to internal modes are always in between ϕ and $\phi+180°$. The loop gains of the system are designed such that for acceleration feedback $\phi=-180°$ and for force feedback $\phi=-90°$, see Fig. 7. This means that, for collocated control, the phases of our example loop gains $L_{\ddot{X}_1,ex}(s)$ and $L_{F_s,ex}(s)$ do not drop below $-180°$. Therefore, the phase of $L_{ex}(s)$ will not drop below $\phi=-180°$, because the phase of $L_{ex}(s)$ is always in between the phases of $L_{\ddot{X}_1,ex}(s)$ and $L_{F_s,ex}(s)$, see Fig. 7. This implies that the closed loop system with TSC is stable.

3.3. Controller design and modeling results

To satisfy all three performance criteria from Section 2.2 simultaneously, acceleration feedback (Section 2) is used for low frequencies and TSC (Section 3.1) is used for high frequencies. TSC restricts the roll-off rate for the acceleration feedback controller to -40 dB/decade (phase $-180°$) and for the force feedback controller to -20 dB/decade (phase $-90°$) at high frequencies.

The acceleration feedback controller from (19) can be used for TSC if the zero at 290 Hz is removed. This zero must be removed to preserve the -40 dB/decade roll-off at high frequencies. The resulting controller reads

$$H_{\ddot{X}_1,TSC}(s) = -\left(K_a+\frac{K_v}{s}\right)\frac{s^2}{s^2+2\zeta_l\omega_l s+\omega_l^2}\frac{\omega_f^2}{s^2+2\zeta_f\omega_f s+\omega_f^2}. \quad (26)$$

The force feedback controller (20) for single-sensor control is not used for TSC, because it has no longer the role of adding virtual mass and sky-hook damping. At low frequencies the controller gain for force feedback must be limited to prevent distortion of the compliance. This is realized by a second-order high-pass filter with a corner frequency of 20 Hz ($\omega_f = 20\cdot 2\pi$ rad/s) and a small relative damping $\zeta_f =$ 0.07. These values are identical to the values of the second-order low-pass filter in (26) to create the same behavior in the drop of the phase angle around 20 Hz. To realize the desired roll-off rate of -20 dB/decade at high

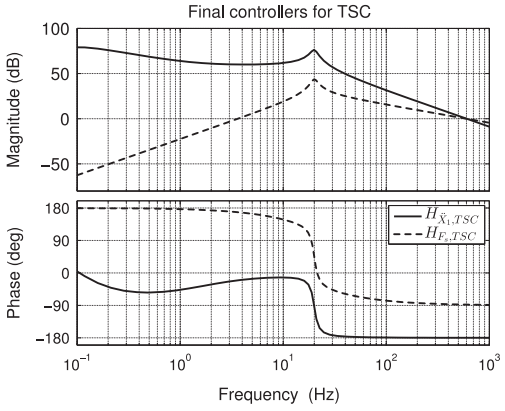

Fig. 8. Bode diagram of the designed controllers for two-sensor control (k_f=20). At low frequencies, acceleration feedback is dominant because force feedback suffers from parasitic stiffness effects. At high frequencies, the 90° out-of-phase property between acceleration feedback and force feedback is obtained.

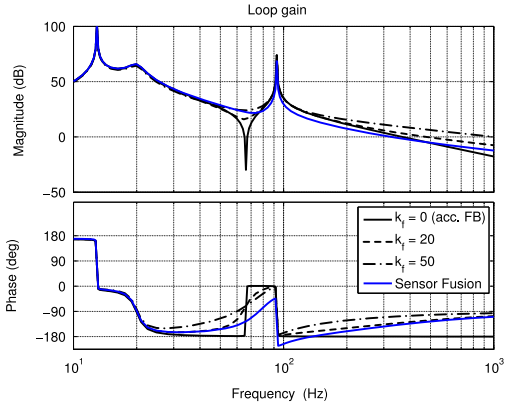

Fig. 10. Bode diagram showing the influence of a varying k_f on the loop gain for two-sensor control. On the one hand, a higher k_f results in more damping of the anti-resonance, but on the other hand also the cross-over frequency increases, resulting in a higher bandwidth of the control system. The figure also shows the loop gain when using sensor fusion. In the latter case, the phase angle crosses the $-180°$ line, which can result in an unstable system.

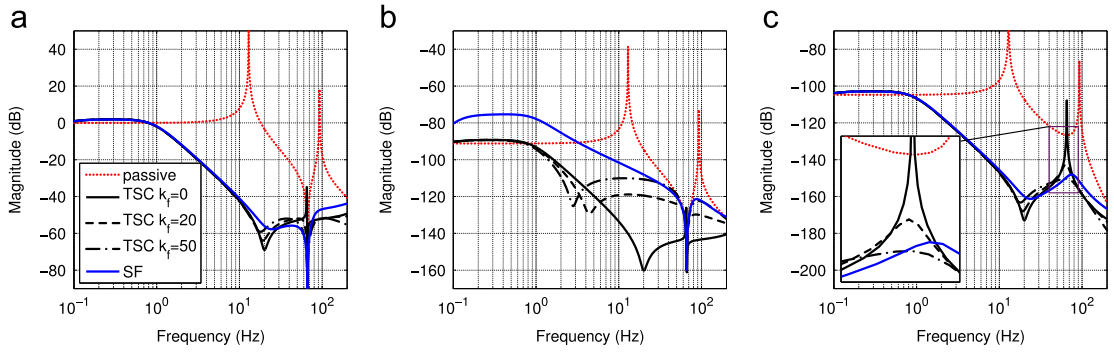

Fig. 9. Bode magnitude plots showing the influence of a varying k_f on the closed loop performance using two-sensor control (TSC), i.e. transmissibility (left), compliance (middle) and deformation transmissibility (right). The line *passive* refers to a passive hard mount vibration isolator, the line *SF* refers to sensor fusion.

frequencies, an additional first-order low-pass filter with a corner frequency of 20 Hz ($\omega_f = 20 \cdot 2\pi$ rad/s) is used. The result is the following force feedback controller:

$$H_{F_s,TSC}(s) = k_f \frac{s^2}{s^2 + 2\zeta_f \omega_f s + \omega_f^2} \frac{\omega_f}{s + \omega_f}. \tag{27}$$

Fig. 8 shows bode plots of controllers (26) and (27). The controller gain k_f can be used to tune the loop gain, see Fig. 10, and the performance, see Fig. 9. The transmissibility is hardly affected by the choice of k_f, see Fig. 9(a). An increased value for k_f results in a higher compliance, see Fig. 9(b), but also in more damping of the internal mode, see Fig. 9(c). From the loop gain plot in Fig. 10 it is observed that an increased value for k_f results in a higher crossover frequency and therefore a higher control bandwidth, but also in more damping of the anti-resonance at 66 Hz (see (23)). The damping of the anti-resonance in the loop gain is coupled to the damping of the internal mode in Fig. 9(c). For the experimental validation described in the next section, the value $k_f = 20$ will be used, since it is a good compromise between damping of the internal mode, the compliance and the controller bandwidth.

3.4. Comparison with sensor fusion

Section 3.3 shows that two-sensor control (TSC) can be used to realize all three performance objectives from Section 2.2 simultaneously. In our previous work (Tjepkema et al., 2011), we showed that Sensor Fusion (SF) leads to similar results for active hard mount systems. The performance of the closed loop system with sensor fusion is also shown in Fig. 9. Using SF as described in Tjepkema et al. (2011), the sensor signals of $\ddot{x}_1$ and F_s are merged using complementary filters (a low-pass filter and high-pass filter of which the sum equals one). Signal $\ddot{x}_1$ is low-pass filtered and F_s is high-pass filtered and scaled with the total machine mass. The merged signal is fed back to a controller similar to (19). This is effectively the same as implementing the following controllers for acceleration and force feedback in the case of sensor fusion:

$$H_{\ddot{X}_1,SF}(s) = H_{\ddot{X}_1,r}(s) \frac{\omega_p}{s + \omega_p}, \tag{28}$$

$$H_{F_s,SF}(s) = \frac{1}{m_1 + m_2} H_{\ddot{X}_1,r}(s) \frac{s}{s + \omega_p} \tag{29}$$

with $H_{\ddot{X}_1,r}(s)$ as described by (19), and ω_p is the corner frequency of the complementary filters. Yet we will show that TSC is preferred over SF.

The first reason to prefer TSC over SF is an enhanced freedom in controller design. TSC is based on a 90° phase-difference between acceleration feedback and force feedback to damp internal modes at high frequencies. Using TSC, the controller structure may be completely different at low frequencies. With SF, the controller structure for acceleration feedback and force feedback is the same in the complete frequency range, except for the complementary filters. Therefore SF has an unnecessary constraint on the controller structure. Due to this unnecessary constraint, the gain of $H_{F_s,SF}(s)$ is much higher than that of $H_{F_s,TSC}(s)$ at low frequencies, resulting in less performance using SF. This is because force feedback increases the compliance at low frequencies, see Fig. 3.

The second reason is the stability property of TSC. It is shown that TSC remains stable as long as the sensors and actuators are collocated, because then the total loop gain never crosses the $-180°$ line. SF does not have this property, because it has a $-180°$ phase crossing of the total loop gain, see Fig. 10. This is caused by the low-pass filter at ω_p in $H_{\ddot{X}_1,SF}(s)$.

The third reason is that TSC can easily be tuned such that multiple internal modes are damped just by realizing a sufficiently high total loop gain. This is in contrast with SF which aims at maximizing the damping of only one internal mode.

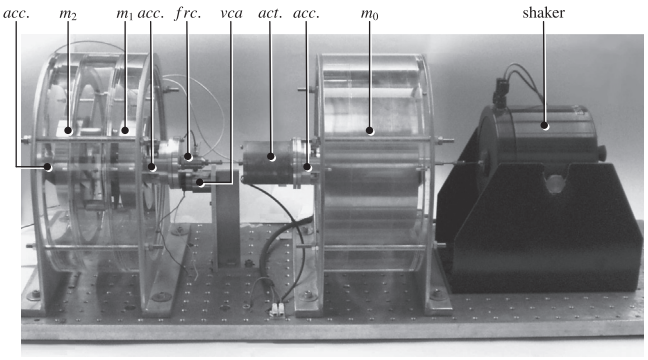

Fig. 11. Experimental setup for the single-axis active vibration isolator. The setup corresponds with the flexible-body model from Fig. 2. The setup is aligned horizontally to prevent gravity compensation.

4. Experimental validation

An experimental setup, that represents the model of Fig. 2, is used to validate the designed controllers. The setup is shown in Fig. 11. In this figure, m_0 is the floor body which can be excited by a shaker. Body m_0 is connected to body m_1 by a mount that consists of a voice coil actuator *act*, generating a force F_a, and a parallel stiffness k_1. Spring k_1 is relatively stiff to represent a hard mount. m_1 and m_2 are machine bodies interconnected by a compliant element with stiffness k_2. The devices *acc.* are piezoelectric accelerometers at m_0, m_1 and m_2. A force sensor *frc.* is mounted between *act* and m_1. An additional voice coil actuator *vca* is used to apply direct disturbance forces to the system. The bodies are mounted in a linear guidance to allow motion in one direction only. To prevent the need for gravity compensation the setup is placed horizontally. Numerical values for the masses and stiffnesses are given in Table 1. The controllers are implemented on a dSpace digital signal processor using a sample frequency of 12 800 Hz. The measurement signals are fed to a charge amplifier containing a band-pass filter with corner frequencies 0.1 Hz and 3 kHz. An additional zero at 680 Hz is used in the controllers to compensate for the induction pole of the voice coil motor. Furthermore the filter frequency ω_l of the high-pass filter in the acceleration feedback controller (26) is increased from 0.1 Hz to 0.3 Hz to circumvent drift in the controller signal. This drift originates from the piezoelectric sensors, which give unreliable measurements at low frequencies.

To determine the (deformation) transmissibility the floor body is excited by a shaker such that the velocity spectrum of body m_0 is 25 μm/s RMS per 1/3 octave, which is comparable to VC-B curve excitation as defined by Gordon (1991). To determine the compliance, a direct disturbance force is applied by the additional voice coil actuator *vca*. This actuator provides a random signal of 0.3 N RMS.

In practical applications it will be hard to measure Δx. For this setup there is an indirect method to measure it. This is because the setup consists of two clearly separated masses m_1 and m_2. By neglecting the parasitic stiffness effects of the linear guidance for mass m_2 and analyzing the equation of motion of m_2 in Fig. 2, which is given by

$$m_2 \ddot{X}_2(s) = -k_2 \Delta X(s), \tag{30}$$

it is observed that Δx can be approximated by scaling $\ddot{x}_2$ by a factor $-m_2/k_2$. Since measuring $\ddot{x}_2$ is much easier than Δx,

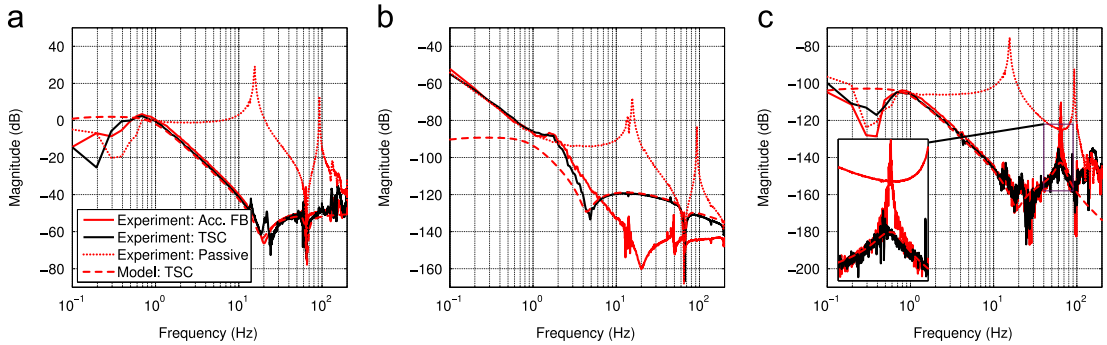

Fig. 12. Bode magnitude plot with experimental results for the closed loop performance, i.e. transmissibility (left), compliance (middle) and deformation transmissibility (right). TSC represents two-sensor control. In the mid-frequency range, the experiment results show a good fit with the model. At low frequencies and high frequencies, sensor noise dominates the figure.

the scaled response of $\ddot{x}_2$ is used to analyze the deformation transmissibility.

The performance objectives are determined by calculating (cross) power spectral densities (PSDs), denoted as $P_{uy}(f)$. Here f is the frequency in Hertz and u,y are the measured signals. The estimated transmissibility $\hat{T}(s)$, compliance $\hat{C}(s)$ and deformation transmissibility $\hat{T_d}(s)$ are calculated by

$$\hat{T}(f)=\frac{P_{\ddot{x}_1\ddot{x}_0}(f)}{P_{\ddot{x}_0\ddot{x}_0}(f)}, \tag{31}$$

$$\hat{C}(f)=\frac{P_{\ddot{x}_1F_d}(f)}{P_{F_dF_d}(f)}\frac{1}{(2\pi f)^2}, \tag{32}$$

$$\hat{T}_d(f)=\frac{P_{\ddot{x}_2\ddot{x}_0}(f)}{P_{\ddot{x}_0\ddot{x}_0}(f)}\frac{m_2}{k_2}. \tag{33}$$

Notice that the compliance is estimated as $\hat{C}(f)=P_{x_1F_d}(f)/P_{F_dF_d}(f)$ in which $P_{x_1F_d}(f)=P_{\ddot{x}_1F_d}(f)/(2\pi f)^2$. This is equal to integrating $P_{\ddot{x}_1F_d}(f)$ twice with respect to time. This estimation is used because it is hard to measure the absolute position x_1 directly.

In Fig. 12 the experimental results are compared to the theoretical values. When evaluating the (deformation) transmissibilities it is observed that the measurements become noisy at frequencies above 100 Hz. This is because sensor noise dominates over the actual acceleration level at these high frequencies. At frequencies below 1 Hz the results become unreliable because the piezoelectric sensors cannot provide reliable measurements below 1 Hz. In the mid-frequency range (1–100 Hz) the measurements fit well with the modeling results. Around 20 Hz some additional peaks due to resonance modes are visible. These modes originate from motion of the table on which the experimental setup is mounted. The force sensor is not able to measure and compensate for this motion, which is transmitted onto the machine bodies by means of the parasitic stiffness path formed by the linear guidance (Tjepkema et al., 2011). This phenomenon is a limitation of the experimental setup and is not expected to occur in practical vibration isolators. In the deformation transmissibility, the internal mode is poorly damped when acceleration feedback is used, while with TSC the mode is damped significantly. As expected from the model, the resonance peak of the internal mode drops down with 30 dB. The compliance plots in Fig. 12(b) show that for high frequencies (>5 Hz) the compliance is very well estimated by the model. At low frequencies, the measured compliance deviates from the modeled compliance and has a certain slope. This is because the measured compliance is derived from the measured acceleration $\ddot{x}_1$ instead of the displacement x_1, see (32). At low frequencies, the actual acceleration level is so small that sensor noise dominates the measurement, so that the measured accelerations no longer represent the actual acceleration level. The compliance is derived from the acceleration response filtered with $1/(2\pi f)^2$, resulting in the slope which is visible in Fig. 12(b) at low frequencies.

5. Discussion

Although the experimental setup used in this paper is a rough simplification of a real precision machine, the results have a generic applicability. The expectation is that in future work the TSC approach in this paper can be extended to multi-axis systems, especially when decoupling control is possible. An example of decoupling control is the modal control approach in van Dijk (2009). When doing so, the multi-axis control problem reduces to a set of SISO control problems which can be solved by the TSC strategy presented in this paper. A similar method is described in our previous work Tjepkema et al. (2011), where we describe a method to implement sensor fusion on more realistic multi-axis systems.

Vibration isolation systems for precision machines usually have to perform well for floor vibrations as small as VC-E curve excitation. However, we used a VC-B curve excitation level to make the effect of two-sensor control more clearly by preventing the limiting effects of sensor noise and actuator noise showing up in the results.

We assumed ideal actuator behavior within the bandwidth of the controller by using a voice coil motor in combination with the high stiffness of the hard mount. Alternatively, piezo stack actuators with an elastic element in series could have been used as described in van der Poel (2010). However, in practice, the actuator will not have an infinite stiffness, which can lead to loss of collocation. Loss of collocation can be problematic because the two-sensor control strategy guarantees stability as long as the system is collocated, see Section 3.2. Linearity of the electronics could also become a problem if the controller bandwidth becomes really high. Using additional filtering could be a simple solution to prevent instability due to parasitic actuator dynamics or nonlinearities in the electronics.

6. Conclusions

Two-sensor control is a promising strategy to damp internal modes in active hard mount systems, while simultaneously obtaining a low transmissibility of floor vibrations and a low compliance. The frequency of the suspension mode is lowered from 13 Hz to 1 Hz and 70% sky-hook damping is added to this mode, while the high static stiffness of the passive hard mount is not affected. Using two-sensor control, damping is added to the

internal mode and the peak value of this resonance is decreased with 30 dB in contrast with single-sensor control using acceleration feedback. The two-sensor control strategy is successfully validated on an experimental setup. Compared to sensor fusion, two-sensor control offers more possibilities for loop shaping and it has better stability properties.

Appendix A. Derivation of the sensitivity function for two-sensor control

In this appendix, a relation is derived between the open loop performance of the internal deformation $\Delta X(s)$ and the closed loop performance in the case of two measurement outputs and one control input. It follows that the closed loop performance equals the open loop performance scaled with the sensitivity function $1/(1+L(s))$, which is the same relation as valid in SISO systems.

Consider the closed loop plant in Fig. 4 with the symbols as defined in Section 3.1. The Laplace operator s is omitted. When neglecting the direct disturbance force F_d, the output ΔX can be written as

$$\Delta X = G_{31}\ddot{X}_0 + G_{33}F_a \tag{A.1}$$

The actuator force equals

$$F_a = -(H_{\ddot{X}_1}\ddot{X}_1 + H_{F_s}F_s) \tag{A.2}$$

The sensor outputs can be expressed as

$$\ddot{X}_1 = G_{11}\ddot{X}_0 + G_{13}F_a \tag{A.3}$$

$$F_s = G_{21}\ddot{X}_0 + G_{23}F_a \tag{A.4}$$

Eqs. (A.3) and (A.4) are substituted into (A.2):

$$F_a = -H_{\ddot{X}_1}(G_{11}\ddot{X}_0 + G_{13}F_a) - H_{F_s}(G_{21}\ddot{X}_0 + G_{23}F_a) \tag{A.5}$$

Rewriting (A.5) gives the closed loop transfer function from floor vibration to actuator force:

$$F_a = -\frac{H_{\ddot{X}_1}G_{11} + H_{F_s}G_{21}}{1 + H_{\ddot{X}_1}G_{13} + H_{F_s}G_{23}}\ddot{X}_0 \tag{A.6}$$

This expression for F_a is substituted into (A.1):

$$\Delta X = \left(G_{31} - G_{33}\frac{H_{\ddot{X}_1}G_{11} + H_{F_s}G_{21}}{1 + H_{\ddot{X}_1}G_{13} + H_{F_s}G_{23}}\right)\ddot{X}_0 \tag{A.7}$$

This means that the closed loop transfer function from floor motion $\ddot{X}_0$ to internal deformation ΔX equals

$$\left(\frac{\Delta X}{\ddot{X}_0}\right)_{\text{c.l.}} = G_{31} - G_{33}\frac{H_{\ddot{X}_1}G_{11} + H_{F_s}G_{21}}{1+L} \tag{A.8}$$

In (A.8) the loop gain $L = H_{\ddot{X}_1}G_{13} + H_{F_s}G_{23}$. To simplify (A.8) a substitution for G_{33} is derived:

$$G_{33} = \frac{\Delta X}{F_a} = \frac{\Delta X}{\ddot{X}_0}\frac{\ddot{X}_1}{F_a}\frac{\ddot{X}_0}{\ddot{X}_1} = G_{31}\frac{G_{13}}{G_{11}} \tag{A.9}$$

Eq. (A.9) is substituted into (A.8):

$$\left(\frac{\Delta X}{\ddot{X}_0}\right)_{\text{c.l.}} = G_{31}\left(1 - \frac{H_{\ddot{X}_1}G_{13} + H_{F_s}G_{21}\dfrac{G_{13}}{G_{11}}}{1+L}\right) \tag{A.10}$$

In a similar way as in (A.9) it can be shown that $G_{21}G_{13}/G_{11} = G_{23}$, which means that the nominator in (A.10) equals L. This leads to the final result:

$$\left(\frac{\Delta X}{\ddot{X}_0}\right)_{\text{c.l.}} = G_{31}\frac{1}{1+L} \tag{A.11}$$

Eq. (A.11) states that the closed loop internal deformation is equal to the open loop internal deformation G_{31} scaled with the sensitivity $1/(1+L)$.

References

Beard, A., Schubert, D., & von Flotow, A. (1994). A practical product implementation of an active/passive vibration isolation system. *Proceedings of the SPIE: Vibration Monitoring Control*, *2264*, 38–49.

El-Sinawi, A. H. (2004). Active vibration isolation of a flexible structure mounted on a vibrating elastic base. *Journal of Sound and Vibration*, *271*(1), 323–337.

Gardonio, P., Elliott, S. J., & Pinnington, R. J. (1997). Active isolation of structural vibration on a multiple-degree-of-freedom system, part II: *Effectiveness of active control strategies*. *Journal of Sound and Vibration*, *207*(1), 95–121.

Gordon, C. D. (1991). Generic criteria for vibration-sensitive equipment. *Proceedings of International Society for Optical Engineering*, *1619*, 71–85.

Hauge, G., & Campbell, M. (2004). Sensors and control of a space-based six-axis vibration isolation system. *Journal of Sound and Vibration*, *269*(3–5).

Heertjes, M., de Graaff, K., & van der Toorn, J. (2005). Active vibration isolation of metrology frames; a modal decoupled control design. *Journal of Vibration and Acoustics*, *127*(3), 223–233.

Holterman, J., & de Vries, T. J. A. (2004). Active damping within an advanced microlithography system using piezoelectric smart discs. *Mechatronics*, *14*(1), 15–34.

Karnopp, D., & Trikha, A. (1969). Comparative study of optimization techniques for shock and vibration isolation. *Transactions of American Society of Mechanical Engineers, Journal of Engineering for Industry*, *91*(4), 1128–1132.

Nelson, P. G. (2002). Supporting active electro-pneumatic vibration isolation systems on platforms supported by STACIS™ hard-mount of piezoelectric isolation systems. ⟨http://www.techmfg.com/pdf/TMC%20STACIS.pdf⟩.

Pantazi, A., Sebastian, A., Pozidis, H., Eleftheriou, E. (2005). Two-sensor-based H_∞ control for nanopositioning in probe storage. In *Proceedings of the44th IEEE conference on decision and control* (pp. 1174–1179).

Rivin, E. I. (2003). *Passive vibration isolation*. New York: ASME-Press.

Tjepkema, D., van Dijk, J., & Soemers, H. M. J. R. (2011). Sensor fusion for active vibration isolation in precision equipment. *Journal of Sound and Vibration*, *331*(4), 735–749.

van der Poel, G. W. (2010). *An exploration of active hard mount vibration isolation for precision equipment* (Ph.D. thesis). Enschede, The Netherlands: University of Twente.

van Dijk, J. (2009). Mechatronic design of hard-mount concepts for precision equipment. In *Motion and vibration control* (pp. 315–324).